Chapter 12

Combustion Catalyst: Nano-Fe_2O_3 and Nano-Thermite Al/Fe_2O_3 with Different Shapes

Ningning Zhao, Jiachen Li, Fengqi Zhao, Ting An, Rongzu Hu and Haixia Ma

Additional information is available at the end of the chapter

http://dx.doi.org/10.5772/64748

Abstract

In order to enable the energetic materials to possess a more powerful performance, adding combustion catalysts is a quite effective method. Granular, oval, and polyhedral Fe_2O_3 particles have been prepared by the hydrothermal method and used to fabricate Al/Fe_2O_3 thermites. All the Fe_2O_3 and Al/Fe_2O_3 thermite samples were characterized using a combination of experimental techniques including scanning electron microscopy (SEM), energy dispersive spectrometer (EDS), X-ray diffraction (XRD), Fourier transform infrared spectroscopy (FTIR), transmission electron microscope (TEM), and high-resolution TEM (HRTEM). The non-isothermal decomposition kinetics of the composites and nitrocellulose (NC) can be modeled by the Avrami-Erofeev equation $f(\alpha)=3(1-\alpha)[-\ln(1-\alpha)]^{1/3}/2$ in differential form. Through the thermogravimetric analysis infrared (TG-IR) analysis of decomposition processes and products, it is speculated that Fe_2O_3 and Al/Fe_2O_3 can effectively accelerate the thermal decomposition reaction rate of NC by promoting the O-NO_2 bond cleavage. Adding oxides or thermites can distinctly increase the burning rate, decrease the burning rate pressure exponent, increase the flame temperature, and improve the combustion wave structures of the ammonium perchlorate/hydroxyl-terminated polybutadiene (AP/HTPB) propellants. Among the three studied, different shapes of Fe_2O_3, the granular Fe_2O_3, and its corresponding thermites (Al/Fe_2O_3(H)) exhibit the highest burning rate due to larger surface area associated with smaller particle size. Moreover, Al/Fe_2O_3(H) thermites have more effective combustion-supporting ability for AP/HTPB propellants than Fe_2O_3 structures and the other two as-prepared Al/Fe_2O_3 thermites.

Keywords: combustion catalyst, thermal decomposition mechanism, combustion wave structure

1. Introduction

Energetic materials (explosives, propellants, and pyrotechnics) are necessary material bases of high-performance weapons and ammunition, which are used extensively for both civil, military, and space applications. In order to enable the energetic materials to possess a more powerful performance, such as the high quantity of heat release, the high combustion temperature, the fast burning rate, and so on, adding combustion catalysts is a quite effective method.

In recent years, researchers pay much attention to the preparation and application of the combustion catalysis of nanoscale. Many studies reported that catalysts in nanoscale exhibit the absolute advantages both in accelerating the thermal decomposition process of the main energetic materials such as cyclotrimethylene trinitramine (RDX), nitrocellulose (NC), cyclotetramethylene tetranitramine (HMX), 2,4,6,8,10,12-hexanitro-2,4,6,8,10,12-hexanitro hexaazaisowurtzitane (CL-20), and 3-nitro-1,2,4-triazol-5-one (NTO), and in enhancing the ignition and combustion performances of the solid. For instance, the nano-sized Cr_2O_3 particles decrease the ignition delay time by a factor 3.5 (16 ± 2 vs 54 ± 4 ms) and accelerate the combustion rate (340 ± 10 mm s^{-1}) of the Al/Cr_2O_3 thermite, which is fabricated by Cr_2O_3 micro- or NPs (Φ ≈20 nm) and Al NPs (Φ ≈50 nm) [1]. Pantoya [2] reported that nanocomposite thermites (Al/MoO_3) can significantly reduce the ignition delay time compared with micron-composite thermites. Nitrocellulose nanofiber-based thermite textiles were studied and compared with the pure nitrocellulose and nano-aluminum incorporated nanofiber; the result indicates that the burning rates were enhanced by adding the Al/CuO thermite [3].

The abovementioned nanothermite contains two parts: metal fuel (Al, used due to its low cost, high density, and the efficient catalytic property [4]) and metal oxides (Fe_2O_3, CuO, MnO_2, MoO_3, PbO [5], Bi_2O_3, etc.). The nanothermite system, as the metastable intermolecular composites (MICs) [6], can enhance the reactivity [7–9] through the oxidation-reduction reactions, which lead to high burning rate [10], high heat production [11], and negligible gas generation. The traditional thermite, Al/Fe_2O_3, is prepared in various nanoparticle size, shape, and composition [12] in order to be better applied in free-standing heat sources, airbag ignition materials, hardware destruction devices, welding torches [13], and energetic material field. Both Al and Fe_2O_3 particles have been used as catalysts not only in the thermal decomposition process of the main energetic components but also in composite solid propellants [14–17]. However, the effects of Al/Fe_2O_3 nanoparticles on the thermal behavior and non-isothermal decomposition kinetics of NC are barely investigated. And, to the best of our knowledge, there has been no report about the dependence of catalytic properties of Al/Fe_2O_3 thermites on the morphology of Fe_2O_3 particles in combustion reactions to date.

Nitrocellulose (NC) is extensively applied as a main component in gun, blasting gelatin, dynamites, and rocket propellants [18–21] owing to its high flammability and explosiveness. In order to obtain more information about NC, the thermal decomposition mechanism of NC has been investigated. It is shown that the fission of oxygen-nitrogen bond is the first and rate-determining step during the decomposition process [22–25]. Quantities of

http://dx.doi.org/10.5772/64748

NO_2 gases, derived from the O-NO_2 bond cleavage, could stagnate in the polymer skeleton and lead to promote the secondary autocatalytic reactions (i.e., the heterogeneous reactions in condensed phase) [26]. Furthermore, Mahajan et al. [27] reported that copper oxide influences the combustion/thermal decomposition of NC in a way so as to retard the breaking of O-NO_2 bonds in solid phase. With the excellent characteristics of nanomaterials, we study the influence of Fe_2O_3 particles and Al/Fe_2O_3 thermites on thermal behavior and non-isothermal decomposition kinetics of NC in order to provide basic data for establishing the combustion model and studying the combustion process.

In this contribution, granular, oval, and polyhedral Fe_2O_3 particles have been prepared by the hydrothermal method and used to fabricate Al/Fe_2O_3 thermites by integrating Al nanopowders with Fe_2O_3 at a stoichiometric ratio of Fe_2O_3:Al (71.1wt%:28.9wt%). All the Fe_2O_3 and Al/Fe_2O_3 thermite samples were characterized using a combination of experimental techniques including scanning electron microscopy (SEM), energy dispersive spectrometer (EDS), X-ray diffraction (XRD), Fourier transform infrared spectroscopy (FTIR), transmission electron microscope (TEM) and high-resolution TEM. The effects of Fe_2O_3 nanoparticles and Al/Fe_2O_3 on the thermal decomposition of NC have been investigated by the differential scanning calorimetry (DSC) method and the thermogravimetry with Fourier transform infrared analysis (TG-IR). The influences of Fe_2O_3 and the corresponding thermite on the combustion properties of the ammonium perchlorate/hydroxyl-terminated polybutadiene (AP/HTPB) composite propellant were investigated and compared. Moreover, the combustion wave structures and the flame temperatures of AP/HTPB composite propellants containing thermites Al/Fe_2O_3 are obtained at 4 MPa.

2. Experimental section

2.1. Synthesis of Fe_2O_3 particles and Al/Fe_2O_3 thermites

The granular, oval, and polyhedral Fe_2O_3 particles were prepared following the procedures developed from our reports [28, 29], and denoted as Fe_2O_3(H), Fe_2O_3(o), and Fe_2O_3(p), respectively. Three corresponding thermites Al/Fe_2O_3(H), Al/Fe_2O_3(o), and Al/Fe_2O_3(p) were prepared [29] with a stoichiometric ratio of Fe_2O_3:Al (71.1wt%:28.9wt%) based on the calculation [30].

2.2. Preparation of Fe_2O_3-NC and Al/Fe_2O_3-NC

The Fe_2O_3 particles or Al/Fe_2O_3 thermite was evenly mixed with NC via grinding to obtain the composite materials, respectively. For the Fe_2O_3-NC composites, the Fe_2O_3:NC mass ratio was 1:1, while for the Al/Fe_2O_3-NC composites it was 1:1, too. The grinding process was maintained for 30 min to obtain light red or dark gray composite materials. The products were used for differential scanning calorimetry experiment, in order to assess the thermal behavior and the effects of Fe_2O_3 particles or Al/Fe_2O_3 on NC.

2.3. Preparation of AP/HTPB propellant formulations

The as-prepared Fe_2O_3(H), Fe_2O_3(o), Fe_2O_3(p), and their corresponding thermites are used as the burning rate modifiers in the preliminary AP/HTPB propellant formulation [29] as shown in **Table 1**.

No.	HTPB system/%	Al/%	Coarse AP/%	Superfine AP/%	Additives	Additives/%
N0	14.3	15.3	18.4	52.0	none	0.0
F1	14.3	15.3	18.4	52.0	Fe_2O_3(H)	2.0
F2	14.3	15.3	18.4	52.0	Fe_2O_3(o)	2.0
F3	14.3	15.3	18.4	52.0	Fe_2O_3(p)	2.0
S1	14.3	14.5	18.4	52.0	Al/Fe_2O_3(H)	2.8
S2	14.3	14.5	18.4	52.0	Al/Fe_2O_3(o)	2.8
S3	14.3	14.5	18.4	52.0	Al/Fe_2O_3(p)	2.8

Table 1. The composition and content of composite propellant.

2.4. Samples characterization

The physical phase, composition, morphology, and structure of materials were characterized by SEM-EDS, TEM, XRD, and FT-IR. X-ray diffractograms were recorded on a D/MAX-3C (Japan) instrument using Cu Kα_1 radiation (λ = 0.15406 nm) at 40-kV voltage and a 40-mA current ranging from 10° to 80°. SEM observations were carried out on a Quanta 400 FE-SEM (FEI Co., USA) at an acceleration voltage of 30 kV. EDS was measured using an INCAIE350 testing device from OXFORD Instruments INC (UK) with a discharge voltage of 4–10 kV and a distance of exactly 1 mm between the electrodes. The morphology and size of as-obtained products were investigated with a transmission electron microscope and high-resolution TEM on a Libra 200FE (Carl Zeiss SMT Pte Ltd., Germany). The sample structure and composition were characterized using Bruker Tensor 27 infrared spectrometer.

The specific surface area was determined with Brunauer-Emmett-Teller (BET) Procedure (Autosorb-1C-TCD, American Quantachrome Instruments).

The thermal behavior of the samples was investigated using DSC (Q2000, TA Co.) at a heating rate of 10°C min^{-1} from room temperature to 300°C in an N_2 atmosphere at a flow rate of 50 mL min^{-1} under ambient atmospheric pressure. To explore the reaction mechanism of the intense exothermic decomposition processes of NC and Fe_2O_3-NC and to obtain the corresponding kinetic parameters (apparent activation energy (E_a/kJ mol^{-1}), pre-exponential constant (A/s^{-1})) and the most probable kinetic model function, the DSC curves at the heating rates of 5.0, 10.0, 15.0, 20.0, 25.0, and 30.0°C min^{-1} were dealt by mathematic means.

The thermal decomposition studies of NC and Fe_2O_3-NC were also performed by the thermogravimetry (Netzsch STA409) with Fourier transform infrared (Brucker V70) analysis technique under nitrogen environment at the heating rate of 10°C min^{-1}.

http://dx.doi.org/10.5772/64748

The thermal behavior of the prepared thermites was carried out on a TA Instrument (Q600) device with a 10°C min^{-1} heating rate, using N_2 with a flow rate of 100 mL min^{-1}.

Burning parameters of AP/HTPB propellant including the rate and the pressure exponent were obtained by acoustic emission method by the AE/BX-2006 multifunction system [29].

3. Structure characterization

3.1. Morphological characterization

The microstructure characterizations of the Fe_2O_3 particles and Al/Fe_2O_3 thermites are determined by analytical SEM as well as TEM.

Figure 1 shows the SEM images of the granular, oval, and polyhedral Fe_2O_3 particles and the corresponding Al/Fe_2O_3 thermite. From **Figure 1(a)**, it can be found that Fe_2O_3(H) particles are granular in shape with a relatively small size (average 200 nm) and seem somewhat aggregated. Fe_2O_3(o) particles (**Figure 1(c)**) have an oval shape and a rough surface morphology due to the adhesion of scrap irons. The shape of Fe_2O_3(p) (**Figure 1(e)**) particles is polyhedral, which is quite different from the other two samples. A closer examination of the SEM images indicates that Fe_2O_3(p) particles are not very uniform in size, agglomerated, and have larger surface-area-to-volume (S/V) ratio than that of Fe_2O_3(o) particles. **Figure 1(b)**, **(d)**, and **(f)** show the SEM images of Al/Fe_2O_3(H), Al/Fe_2O_3(o), and Al/Fe_2O_3(p), respectively. Some degree of aggregation can be found in the three thermite systems. Also, there seems to be favorable interfacial between Al and Fe_2O_3 particles.

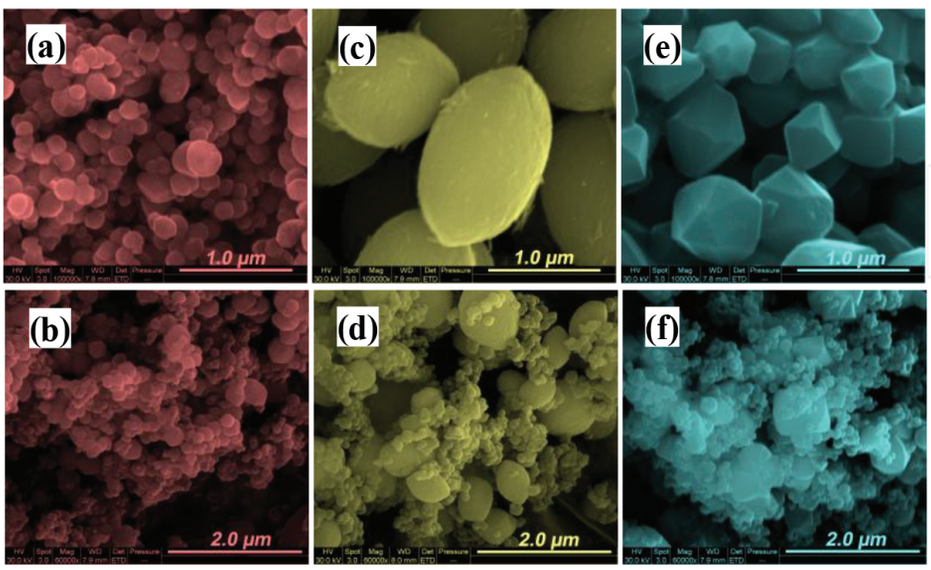

Figure 1. SEM images of Fe_2O_3 (×100,000 magnification) and thermites Al/Fe_2O_3 (×60,000 magnification). (a) Fe_2O_3(H), (b) Al/Fe_2O_3(H), (c) Fe_2O_3(o), (d) Al/Fe_2O_3(o), (e) Fe_2O_3(p), and (f) Al/Fe_2O_3(p).

Investigations of the low-magnification TEM image (**Figure 2(b)**) of Fe_2O_3(H) nanoparticles indicate that most of the particles have an irregular sphere geometrical structure, and usually possess rough surfaces. Typical HRTEM images of the small part of Fe_2O_3(H) nanoparticles were obtained and are shown in **Figure 2(b)**, **(c)**, and **(d)**. Just one set of clear lattice fringes with the interplanar distance of 0.25 nm could be seen in **Figure 2(b)**, **(d)**, inset (i), and (v), which can be indexed to the (110) plane of rhombohedral Fe_2O_3(H) structure. Excellent crystallinity is also confirmed by corresponding fast Fourier-transform (FFT) transformation (inset in **Figure 2**(iii)).

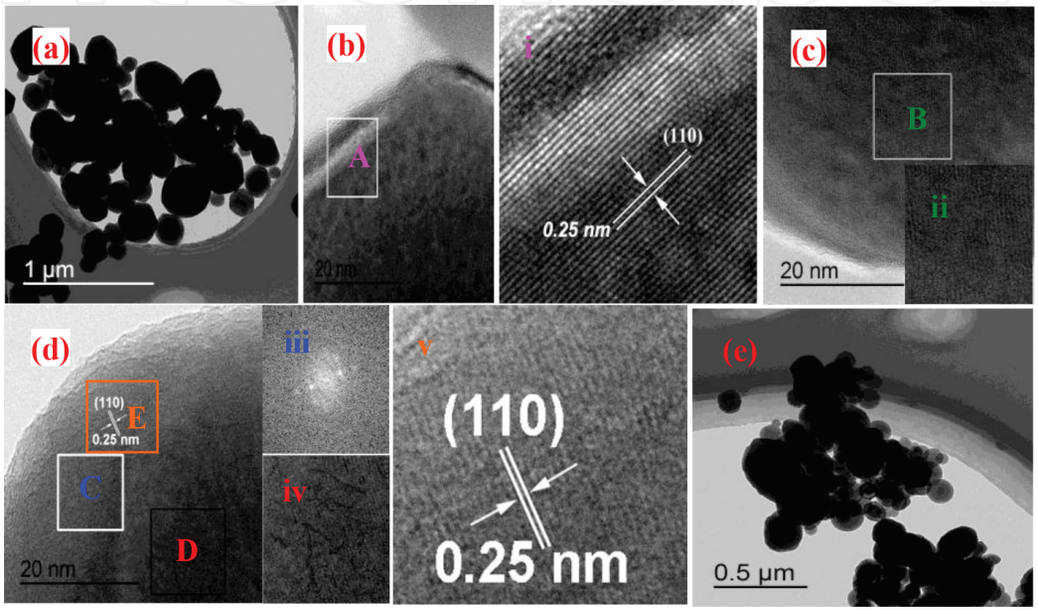

Figure 2. (a) and (e) show TEM images of Fe_2O_3(H) and Al/Fe_2O_3(H), respectively; (b, c, d) HRTEM images of Fe_2O_3(H) nanoparticles. Insets i and v are the high-resolution images of Fe_2O_3(H) nanoparticles, insets ii and iv show a high-resolution image of Fe_2O_3(H) nanoparticles containing stacking faults and dislocation tangles/networks on the surface, respectively, and inset iii shows the corresponding fast Fourier-transform (FFT) pattern of Fe_2O_3(H) nanoparticles.

Particles containing a certain extent of lattice defects such as dislocation and stacking fault caused by the high pressure, temperature, and concentration through the hydrothermal treatment have also been found. **Figure 2(c)** gives an example of a series of diagonal and straight-stacking faults within a particle throughout most of the surface. It can be seen more clearly in an enlargement of a local region (inset ii). **Figure 2(d)**, the area "D" marked black pane and the corresponding inset (iv), shows a high-resolution image of the Fe_2O_3(H) nanoparticles containing dislocation tangles/networks on the surface. These linear and plane defects mentioned above have profound effects on the growth and property of the Fe_2O_3(H) nanoparticles [31, 32].

Figure 3 shows the oval Fe_2O_3(o) particles with the length-to-diameter ratio (L/D ratio) of 1.47–1.59. From **Figure 4(b)**, it is really easy to find out the rough surface of Fe_2O_3(o) particle, which is consistent with the SEM measurement. In the TEM image of Al/Fe_2O_3(o) thermites, the small spherical Al nanoparticles stick together, and also with the Fe_2O_3(o) particles.

http://dx.doi.org/10.5772/64748

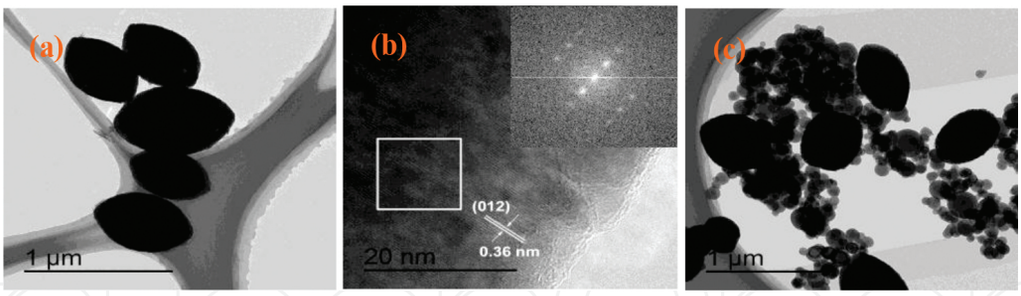

Figure 3. (a) and (c) show TEM images of Fe_2O_3(o) and Al/Fe_2O_3(o), respectively; (b) HRTEM image of Fe_2O_3(o) and the corresponding fast FFT pattern (inset).

Figure 4(a) and **(c)** show the TEM images of the Fe_2O_3(p) and Al/Fe_2O_3(p), respectively. It is obvious to see that almost all of the Fe_2O_3(p) particles are polyhedral in shape, which adhere to the Al particles as seen in **Figure 4(c)**. The corresponding selected area electron diffraction (SAED) pattern shown in **Figure 4(b)** indicates that the Fe_2O_3(p) particles are single crystals. **Figure 4(d)** shows the fringes with the interplanar distance of 0.25 nm in a typical HRTEM image of a Fe_2O_3(p) particle, which agree well with the (110) lattice spacing of the rhombohedral hematite.

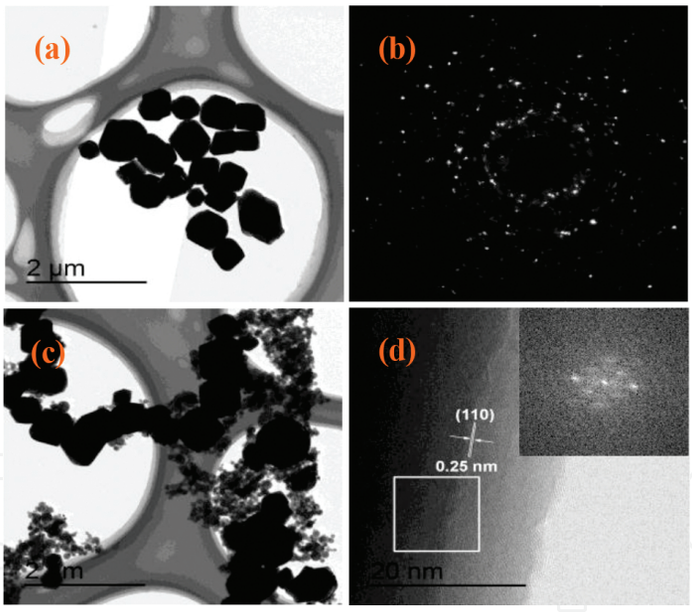

Figure 4. (a) and (c) show TEM images of Fe_2O_3(p) and Al/Fe_2O_3(p), respectively, (b) Selected area electron diffraction (SAED) pattern of Fe_2O_3(p) and (d) HRTEM image of Fe_2O_3(p) and the corresponding fast FFT pattern (inset).

Figures 5–7 show the SEM images of Fe_2O_3(H), Fe_2O_3(p), Fe_2O_3(o), and the corresponding Al/Fe_2O_3, respectively. Take **Figure 5**, for instance. The SEM observation of Fe_2O_3(H)-NC and Al/Fe_2O_3(H)-NC in **Figure 5** shows that the two composites have rough, irregular surface morphology under low magnification, probably due to the agglomeration of Fe_2O_3(H) nanoparticles or Al/Fe_2O_3(H). From **Figure 5(a)** and **(c)**, it can be found that the vast majority

of Fe_2O_3(H) particles or Al/Fe_2O_3(H) adhered on the surfaces of NC short fibers. Also, some small Fe_2O_3(H) (or Al/Fe_2O_3(H)) agglomeration and NC fragments can be observed. The enlargement of a local region on the surface of Fe_2O_3-NC and Al/Fe_2O_3(H)-NC in **Figure 2(b)** and **(d)** indicates that the mechanical-grinding treatment has not changed the basic shape and particle size of Fe_2O_3 and Al.

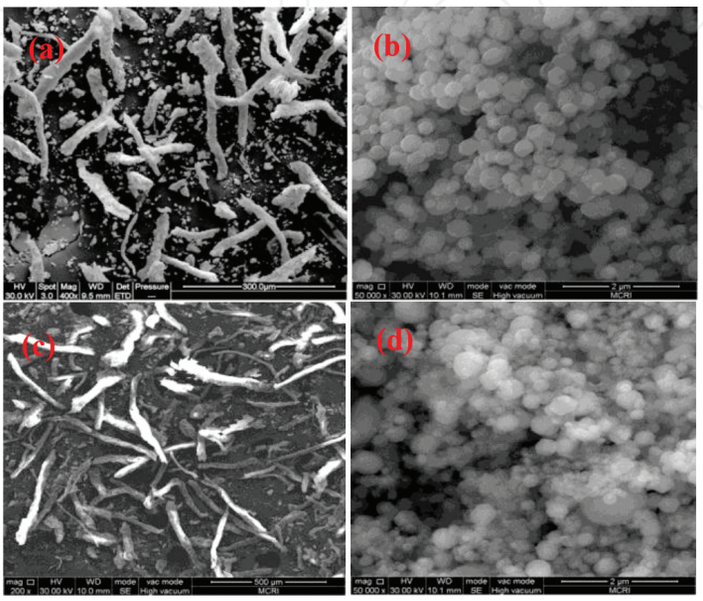

Figure 5. SEM images of Fe_2O_3(H)-NC and Al/Fe_2O_3(H)-NC. (a) Fe_2O_3(H)-NC (×400 magnification), (b) Fe_2O_3(H)-NC (×50,000 magnification), (c) Al/Fe_2O_3(H)-NC (×200 magnification), and (d) Al/Fe_2O_3(H)-NC (×50,000 magnification).

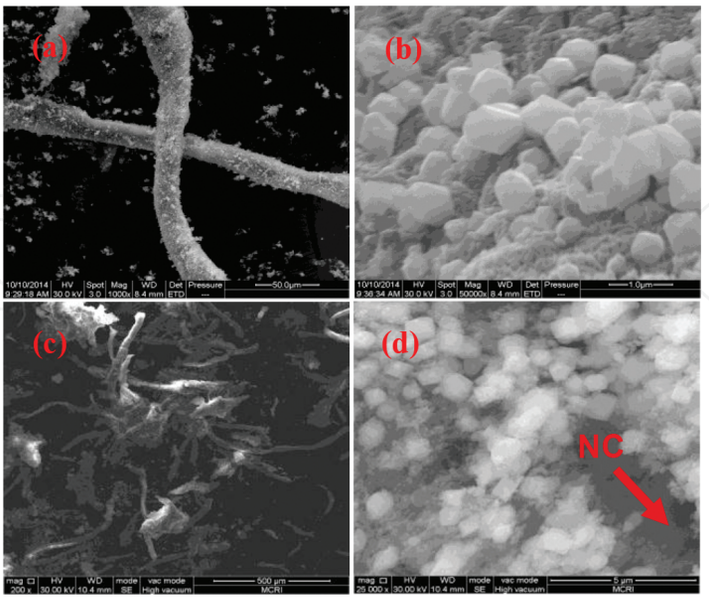

Figure 6. SEM images of Fe_2O_3(p)-NC and Al/Fe_2O_3(p)-NC. (a) Fe_2O_3(p)-NC (×1000 magnification), (b) Fe_2O_3(p)-NC (×50,000 magnification), (c) Al/Fe_2O_3(p)-NC (×200 magnification), and (d) Al/Fe_2O_3(p)-NC (×25,000 magnification).

http://dx.doi.org/10.5772/64748

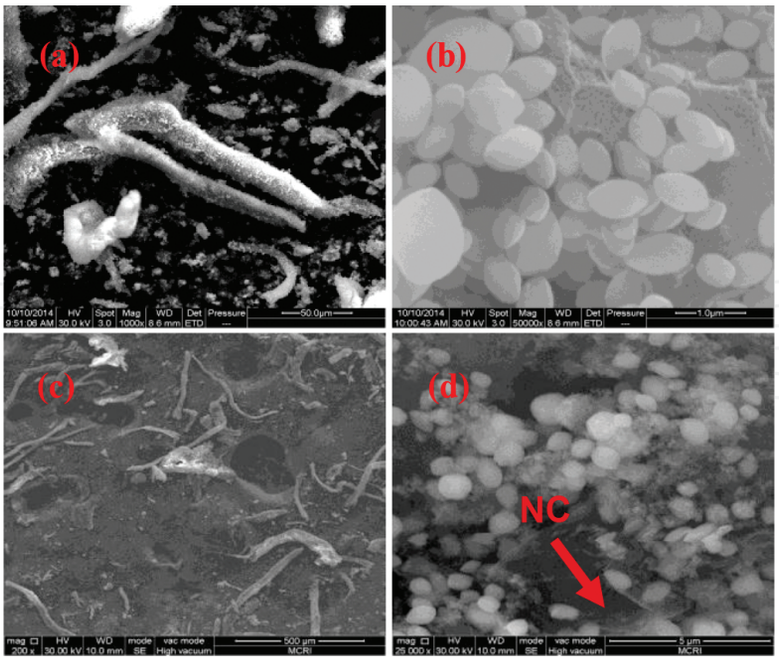

Figure 7. SEM images of Fe_2O_3(o)-NC and Al/Fe_2O_3(o)-NC. (a) Fe_2O_3(o)-NC (×1000 magnification), (b) Fe_2O_3(o)-NC (×50,000 magnification), (c) Al/Fe_2O_3(o)-NC (×200 magnification), and (d) Al/Fe_2O_3(o)-NC (×25,000 magnification).

3.2. Structure and composition

Structure and composition of Fe_2O_3 and thermite were characterized using EDS, XRD, and FTIR techniques. The results [29] show that the three prepared iron oxides are Fe_2O_3 with a stoichiometric ratio of O:Fe (3:2), because their typical XRD patterns coincided with JCPDS: 33-0664, and the hematite lattice vibration is identified at 480 and 571 cm^{-1} [33]. The EDS data show that the thermite samples contain Al element. XRD patterns of thermites reveal no reaction between Al (JCPDS: 65-2869) and Fe_2O_3. It can be found that the presence of water peaks in FTIR spectra of thermites, which is a common phenomenon in the nanomaterials [34–38] especially with the presence of Al particles.

4. Thermal analysis

To explore the reaction mechanism of the intense exothermic decomposition process of NC, Fe_2O_3(H)-NC, and Al/Fe_2O_3(H)-NC and to obtain the corresponding kinetic parameters (apparent activation energy (E_a/kJ mol^{-1}), pre-exponential constant (A/s^{-1})) and the most probable kinetic model functions, the DSC curves at six heating rates of 5.0, 10.0, 15.0, 20.0, 25.0, and 30.0°C min^{-1} were dealt by mathematic means, and the temperature data corresponding to the conversion degrees (α) were found. The values of E_α were obtained by Ozawa's method from the iso-conversional DSC curves at the heating rates of 5.0, 10.0, 15.0, 20.0, 25.0, and 30.0°C min^{-1}, and the E_α-α relation is shown in **Figure 8**. From **Figure 8**, one can see that

the activation energy slightly changes in the section of 0.10–0.80 (α), and the ranges were selected to calculate the non-isothermal reaction kinetics parameters.

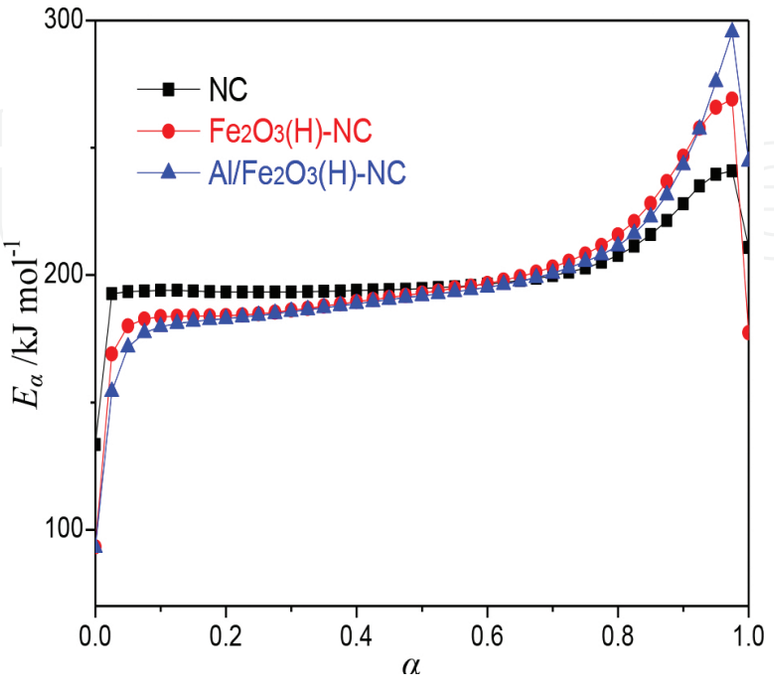

Figure 8. E_α versus α curve of NC, Fe_2O_3(H)-NC, and Al/Fe_2O_3(H)-NC by Flynn-Wall-Ozawa's method.

Six integral methods (MacCallum-Tanner, Šatava-Šesták, Agrawal, general integral, universal integral, and Flynn-Wall-Ozawa) and one differential method (Kissinger) were employed [39–43]. Forty-one types of kinetic model functions and the basic data were put into the integral and differential equations for calculation. The kinetic parameters and the probable kinetic model function were selected by the logical choice method and satisfying the ordinary range of the thermal decomposition kinetic parameters for energetic materials (E_a = 80–250 kJ mol^{-1}, log$A$ = 7–30 s^{-1}). These data together with their appropriate values of linear correlation coefficient (r), standard mean square deviation (Q), and believable factor (d, where $d = (1–r)Q$) are presented in **Tables 2–4**. The values of E_a and log$A$ obtained from each single non-isothermal DSC curve are in good agreement with the calculated values obtained by Kissinger's method and Ozawa's method. We consider the Fe_2O_3-NC composites as an example, and conclude that the reaction mechanism of the intense exothermic decomposition process of Fe_2O_3-NC is classified as Avrami-Erofeev equation $G(\alpha)$=[–ln(1–α)]$^{2/3}$. Substituting $f(\alpha)$ with 3(1–α)[–ln(1–α)]$^{1/3}$/2, E_a with 192.11 kJ mol^{-1}, and A with $10^{18.54}$ s^{-1} in Eq. (1),

$$\frac{\mathrm{d}\alpha}{\mathrm{d}T} = \frac{A}{\beta} f(\alpha) e^{-E/RT} \tag{1}$$

where $f(\alpha)$ and dα/dT are the differential model function and the rate of conversion, respectively.

http://dx.doi.org/10.5772/64748

Method	β/°C min^{-1}	E_a/kJ mol^{-1}	log (A/s^{-1})	r	S	d
MacCallum-Tanner	5	207.98	20.55	0.9983	4.45×10^{-4}	7.50×10^{-7}
	10	205.40	20.25	0.9984	4.11×10^{-4}	6.38×10^{-7}
	15	209.33	20.68	0.9988	3.25×10^{-4}	3.98×10^{-7}
	20	209.34	20.67	0.9987	3.49×10^{-4}	4.61×10^{-7}
	25	211.75	20.91	0.9990	2.56×10^{-4}	2.48×10^{-7}
	30	210.10	20.76	0.9982	4.69×10^{-4}	8.30×10^{-7}
Šatava-Šesták	5	204.55	20.23	0.9983	4.45×10^{-4}	7.50×10^{-7}
	10	202.12	19.94	0.9984	4.11×10^{-4}	6.38×10^{-7}
	15	205.83	20.35	0.9988	3.25×10^{-4}	3.98×10^{-7}
	20	205.83	20.33	0.9987	3.49×10^{-4}	4.61×10^{-7}
	25	208.11	20.56	0.9990	2.56×10^{-4}	2.48×10^{-7}
	30	206.56	20.42	0.9982	4.69×10^{-4}	8.30×10^{-7}
Agrawal	5	207.20	20.49	0.9982	2.37×10^{-3}	4.30×10^{-6}
	10	204.54	20.18	0.9983	2.19×10^{-3}	3.67×10^{-6}
	15	208.37	20.60	0.9987	1.73×10^{-3}	2.29×10^{-6}
	20	208.33	20.58	0.9986	1.86×10^{-3}	2.65×10^{-6}
	25	210.68	20.81	0.9990	1.36×10^{-3}	4.43×10^{-6}
	30	209.03	20.66	0.9981	2.49×10^{-3}	4.77×10^{-6}
General integral	5	205.81	18.98	0.9985	2.36×10^{-3}	4.33×10^{-6}
	10	203.30	18.69	0.9983	2.18×10^{-3}	3.69×10^{-6}
	15	207.22	19.10	0.9987	1.72×10^{-3}	2.30×10^{-6}
	20	207.24	19.09	0.9986	1.85×10^{-3}	2.66×10^{-6}
	25	209.64	19.33	0.9989	1.36×10^{-3}	4.43×10^{-6}
	30	208.02	19.18	0.9981	2.48×10^{-3}	4.79×10^{-6}
Universal integral	5	207.20	20.49	0.9982	2.37×10^{-3}	4.30×10^{-6}
	10	204.54	20.19	0.9983	2.19×10^{-3}	3.67×10^{-6}
	15	208.37	20.60	0.9987	1.73×10^{-3}	2.29×10^{-6}
	20	208.33	20.58	0.9986	1.86×10^{-3}	2.65×10^{-6}
	25	210.68	20.82	0.9990	1.36×10^{-3}	4.43×10^{-6}
	30	209.03	20.66	0.9981	2.49×10^{-3}	4.77×10^{-6}
Mean		207.48	20.22			
Flynn-Wall-Ozawa		185.68 (E_{eo})		0.9998		
		197.56 (E_{po})		0.9979		
Kissinger		199.68 (E_K)	19.82	0.9977		
Mean (E_{eO}, E_{pO}, E_K)		194.31				

Note: E with the subscript of eo and po is the apparent activation energy obtained from the onset temperature (T_e) and the peak temperature (T_p) by Ozawa's method, E with the subscript of K is the apparent activation energy obtained from the peak temperature (T_p) by Kissinger's method.

Table 2. Calculated values of kinetic parameters of decomposition reaction for NC.

Method	β/°C min^{-1}	E_a/kJ mol^{-1}	log(A/s^{-1})	r	Q	d
MacCallum-Tanner	5.0	182.76	17.71	0.9888	4.32×10^{-2}	4.82×10^{-4}
	10.0	190.67	18.63	0.9913	3.36×10^{-2}	2.92×10^{-4}
	15.0	178.17	17.25	0.9949	1.97×10^{-2}	1.00×10^{-4}
	20.0	196.93	19.31	0.9934	2.58×10^{-2}	1.72×10^{-4}
	25.0	203.11	19.97	0.9940	2.32×10^{-2}	1.38×10^{-4}
	30.0	208.59	20.60	0.9946	2.08×10^{-2}	1.11×10^{-4}
Šatava-Šesták	5.0	180.74	17.53	0.9888	4.32×10^{-2}	4.82×10^{-4}
	10.0	188.21	18.40	0.9913	3.36×10^{-2}	2.92×10^{-4}
	15.0	176.41	17.10	0.9949	1.97×10^{-2}	1.00×10^{-4}
	20.0	194.12	19.04	0.9934	2.58×10^{-2}	1.72×10^{-4}
	25.0	199.95	19.67	0.9940	2.32×10^{-2}	1.38×10^{-4}
	30.0	205.38	20.27	0.9946	2.08×10^{-2}	1.11×10^{-4}
Agrawal	5.0	182.16	17.69	0.9878	2.30×10^{-1}	2.80×10^{-3}
	10.0	189.92	18.58	0.9906	1.79×10^{-1}	1.69×10^{-3}
	15.0	177.45	17.22	0.9944	1.05×10^{-2}	5.88×10^{-4}
	20.0	196.02	19.24	0.9928	1.37×10^{-1}	9.95×10^{-4}
	25.0	202.11	19.89	0.9935	1.23×10^{-1}	7.90×10^{-4}
	30.0	206.79	20.51	0.9942	1.11×10^{-1}	6.44×10^{-4}
General integral	5.0	180.77	16.22	0.9877	2.29×10^{-1}	2.81×10^{-3}
	10.0	188.67	17.11	0.9905	1.78×10^{-1}	1.70×10^{-3}
	15.0	176.27	15.79	0.9944	1.05×10^{-1}	5.87×10^{-4}
	20.0	194.91	17.78	0.9927	1.37×10^{-1}	9.95×10^{-4}
	25.0	201.06	18.42	0.9935	1.23×10^{-1}	7.98×10^{-4}
	30	206.78	19.03	0.9942	1.10×10^{-1}	6.43×10^{-4}
Universal integral	5.0	182.16	17.69	0.9878	2.30×10^{-1}	2.80×10^{-3}
	10.0	189.92	18.58	0.9906	1.79×10^{-1}	1.69×10^{-3}
	15.0	177.45	17.22	0.9944	1.53×10^{-1}	4.88×10^{-4}
	20.0	196.02	19.24	0.9928	1.37×10^{-1}	9.95×10^{-4}
	25.0	202.11	19.89	0.9935	1.23×10^{-1}	7.99×10^{-4}
	30.0	207.79	20.51	0.9942	1.11×10^{-1}	6.44×10^{-4}
Mean		192.11	18.54			
Flynn-Wall-Ozawa		188.33 (E_{po})		0.9993		
Kissinger		189.98 (E_K)	18.76	0.9992		
Mean (E_{eO},E_{pO}, E_K)		189.16				

Note: E with the subscript of eo and po is the apparent activation energy obtained from the onset temperature (T_e) and the peak temperature (T_p) by Ozawa's method, E with the subscript of K is the apparent activation energy obtained from the peak temperature (T_p) by Kissinger's method.

Table 3. Calculated values of kinetic parameters of decomposition reaction for Fe_2O_3(H)-NC.

http://dx.doi.org/10.5772/64748

Method	β/°C min^{-1}	E_a/kJ mol^{-1}	log(A/s^{-1})	r	S	d
MacCallum-Tanner	5	174.56	16.81	0.9958	2.84×10^{-3}	1.21×10^{-5}
	10	178.30	17.27	0.9967	2.22×10^{-3}	7.36×10^{-6}
	15	185.26	18.04	0.9971	1.94×10^{-3}	5.61×10^{-6}
	20	183.79	17.87	0.9969	2.10×10^{-3}	6.59×10^{-6}
	25	207.72	20.50	0.9965	2.33×10^{-3}	8.11×10^{-6}
	30	195.50	19.15	0.9962	2.53×10^{-3}	9.56×10^{-6}
Šatava-Šesták	5	173.00	16.67	0.9958	2.84×10^{-3}	1.21×10^{-5}
	10	176.53	17.11	0.9967	2.22×10^{-3}	7.36×10^{-6}
	15	183.10	17.84	0.9971	1.94×10^{-3}	5.61×10^{-6}
	20	181.71	17.68	0.9969	2.10×10^{-3}	6.59×10^{-6}
	25	204.31	20.18	0.9965	2.33×10^{-3}	8.11×10^{-6}
	30	192.76	18.89	0.9962	2.53×10^{-3}	9.56×10^{-6}
Agrawal	5	174.00	16.79	0.9953	1.51×10^{-2}	7.04×10^{-5}
	10	177.61	17.24	0.9964	1.18×10^{-2}	4.29×10^{-5}
	15	184.45	17.99	0.9968	1.03×10^{-2}	3.26×10^{-5}
	20	182.94	17.82	0.9966	1.12×10^{-2}	3.84×10^{-5}
	25	206.67	20.42	0.9962	1.24×10^{-2}	4.67×10^{-5}
	30	194.49	19.07	0.9959	1.34×10^{-2}	5.53×10^{-5}
General integral	5	174.00	16.79	0.9953	1.51×10^{-2}	7.04×10^{-5}
	10	177.61	17.24	0.9964	1.18×10^{-2}	4.29×10^{-5}
	15	184.45	17.99	0.9968	1.03×10^{-2}	3.26×10^{-5}
	20	182.94	17.82	0.9966	1.12×10^{-2}	3.84×10^{-5}
	25	206.67	20.42	0.9962	1.24×10^{-2}	4.67×10^{-5}
	30	194.49	19.07	0.9959	1.34×10^{-2}	5.53×10^{-5}
Universal integral	5	172.64	15.35	0.9953	1.51×10^{-2}	7.09×10^{-5}
	10	176.39	15.80	0.9963	1.17×10^{-2}	4.31×10^{-5}
	15	183.32	16.55	0.9968	1.03×10^{-2}	3.27×10^{-5}
	20	181.88	16.39	0.9965	1.11×10^{-2}	3.85×10^{-5}
	25	205.65	18.94	0.9962	1.23×10^{-2}	4.68×10^{-5}
	30	193.52	17.63	0.9959	1.34×10^{-2}	5.53×10^{-5}
Mean		186.34	17.91			
Flynn-Wall-Ozawa		172.66(E_{eo})		0.9941	4.87×10^{-3}	
		194.23(E_{po})		0.9990	8.60×10^{-4}	
Kissinger		196.18(E_K)	19.44	0.9989	4.56×10^{-3}	
Mean(E_{eO},E_{pO}, E_K)		187.69				

Note: E with the subscript of eo and po is the apparent activation energy obtained from the onset temperature (T_e) and the peak temperature (T_p) by Ozawa's method, E with the subscript of K is the apparent activation energy obtained from the peak temperature (T_p) by Kissinger's method.

Table 4. Calculated values of kinetic parameters of decomposition reaction for Al/Fe_2O_3(H)-NC.

The kinetic equation of the exothermic decomposition reaction may be described as

$$\frac{\mathrm{d}\alpha}{\mathrm{d}T} = \frac{10^{18.71}}{\beta}(1-\alpha)\left[-\ln(1-\alpha)\right]^{1/3}\exp\left(-2.31\times10^{4}/T\right) \tag{2}$$

The values (T_{e0} and T_{p0}) of the onset temperature (T_e) and peak temperature (T_p) corresponding to $\beta\rightarrow0$ were obtained by Eq. (3), and the self-accelerating decomposition temperature (T_{SADT}) was obtained by Eq. (5) [39–43]. The values (T_{SADT} and T_{p0}) are 182.03 and 194.10°C, respectively.

$$T_{e(\mathrm{or\ p})} = T_{e0(\mathrm{or\ p})} + a\beta_i + b\beta_i^2 + c\beta_i^3\ i=1-4 \tag{3}$$

where *a*, *b*, and *c* are coefficients.

$$T_{SADT} = T_{e0} \tag{4}$$

The thermal ignition temperature (T_{be0} or T_{TIT}) was obtained by substituting E_{eo} and T_{e0} into the equation of Zhang et al. (Eq. (5)) [44], and the critical temperatures of thermal explosion (T_{bp0} or T_b) were obtained by substituting E_{po} and T_{p0} in Eq. (5). The values (T_{TIT} and T_b) are 191.44 and 204.16°C, respectively,

$$T_{be0(\mathrm{or\ bp0})} = \frac{E_o - \sqrt{E_o^2 - 4E_oRT_{e0(\mathrm{or\ p0})}}}{2R} \tag{5}$$

The thermal behaviors of NC are also analyzed with the same method using the data in **Figure 8**. The results show that the reaction mechanism of the intense exothermic decomposition process of them is classified as reaction order $f(\alpha) = 3(1-\alpha)[-\ln(1-\alpha)]^{1/3}/2$, $G(a) = [-\ln(1-\alpha)]^{2/3}$. The DSC curves of Fe_2O_3(p)-NC, Al/Fe_2O_3(p)-NC, Fe_2O_3(o)-NC, and Al/Fe_2O_3(o)-NC at a heating rate of 10°C min^{-1} are listed in Figures S1 and S3 (Supplementary data), respectively. The E_α-α relations of Fe_2O_3(p)-NC, Al/Fe_2O_3(p)-NC, Fe_2O_3(o)-NC, and Al/Fe_2O_3(o)-NC are shown in Figures S2 and S4 (Supplementary data). **Table 5** and the supplementary data (Tables S1–S4) show the calculated values of kinetic parameters of decomposition reaction for NC, Fe_2O_3(H)-NC, Al/Fe_2O_3(H)-NC, Fe_2O_3(p)-NC, Al/Fe_2O_3(p)-NC, Fe_2O_3(o)-NC, and Al/Fe_2O_3(o)-NC. From **Table 5**, it can be found that (1) the E_a values of NC-based composites containing Fe_2O_3 and Al/Fe_2O_3 are less than that of NC; (2) the E_a value of NC-based composites containing Al/Fe_2O_3 is less than that of NC-based composites containing the corresponding Fe_2O_3; (3) among the three Fe_2O_3 particles, Fe_2O_3(H) is the best catalyst because E_a of Fe_2O_3(H)-NC is the lowest; (4) the E_a value of Al/Fe_2O_3(o)-NC is 0.16 and 5.57 kJ mol^{-1} lower than that of Al/Fe_2O_3(H)-NC and Al/Fe_2O_3(p)-NC, respectively, but the thermal ignition temperature and the critical temperature of thermal explosion of Al/Fe_2O_3(o)-NC are so high. Therefore, the

prepared Fe_2O_3(H) and Al/Fe_2O_3(H) are the two kinds of promising catalysts developed in accelerating the decomposition rate or the process of NC.

Sample	E_a/kJ mol^{-1}	log(A/s^{-1})	T_{e0}/°C	T_{p0}/°C	T_{be0}/°C	T_{bp0}/°C	$\Delta S^{\neq}$/J·mol^{-1}·K^{-1}	$\Delta H^{\neq}$/kJ·mol^{-1}	$\Delta G^{\neq}$/kJ·mol^{-1}
NC	207.48	20.22	181.76	197.00	191.42	206.69	138.40	199.68	134.61
Fe_2O_3(H)-NC	192.11	18.54	182.03	194.10	191.44	204.16	106.21	189.98	140.35
Al/Fe_2O_3(H)-NC	186.34	17.91	175.57	190.02	185.71	199.59	94.31	196.18	152.46
Fe_2O_3(p)-NC	200.67	19.45	176.38	196.42	185.53	206.82	123.72	185.65	127.56
Al/Fe_2O_3(p)-NC	191.75	18.51	180.29	195.55	190.25	205.52	106.31	185.39	135.56
Fe_2O_3(o)-NC	202.69	19.68	178.87	187.64	187.93	197.14	128.29	195.50	136.39
Al/Fe_2O_3(o)-NC	186.18	17.87	179.82	191.87	189.39	201.97	93.50	187.43	143.95

Table 5. Calculated values of kinetic parameters of decomposition reaction for NC, Fe_2O_3(H)-NC, Al/Fe_2O_3(H)-NC, Fe_2O_3(p)-NC, Al/Fe_2O_3(p)-NC, Fe_2O_3(o)-NC, and Al/Fe_2O_3(o)-NC.

By thermal analysis, the addition of Fe_2O_3(H) and Al/Fe_2O_3(H) did not change the kinetic model function of NC, reduced the value of $E_{a,}$ and the critical temperature of thermal explosion, thus Fe_2O_3(H) nanoparticles and Al/Fe_2O_3(H) thermites could accelerate the decomposition rate or process of NC. Furthermore, the effects of Fe_2O_3(H) nanoparticles and Al/Fe_2O_3(H) on the thermal decomposition of NC have been investigated by the thermogravimetry with Fourier transform infrared analysis (TG-IR).

The TG-IR-hyphenated technique is a highly preferred approach for investigating the thermal degradation of energetic materials. The TG-thermogravimetric derivative (TG-DTG) curves of NC, Fe_2O_3(H)-NC, and Al/Fe_2O_3(H)-NC at a heating rate of 10°C/min are presented in **Figure 9**. Just one stage of the total mass loss can be found from the decomposition processes of NC, Fe_2O_3(H)-NC, and Al/Fe_2O_3(H)-NC. The total weight loss of NC is 68.41%, while that of Fe_2O_3(H)-NC and Al/Fe_2O_3(H)-NC are about 34.77 and 31.12%, respectively, which is lower than that of NC due to the remaining Fe_2O_3 and some residues.

A series of temperature values of typical points including the initial decomposition temperature (T_i), the extrapolated onset temperature (T_e), the peak temperature (T_L), the extrapolated end temperature (T_c), and the final temperature (T_f) deserve special attention. Compared with the degradation process of NC, these typical temperature values of Fe_2O_3(H)-NC and Al/Fe_2O_3(H)-NC obviously are reduced under the influence of Fe_2O_3(H) nanoparticles and Al/Fe_2O_3(H) as seen in **Figure 9(b)** and **(c)**. The peak temperatures of NC, Fe_2O_3(H)-NC, and Al/Fe_2O_3(H)-NC are 209.43, 208.59, and 210.24°C, respectively.

The apparent variation of IR characteristic absorption peaks of the gaseous decomposition products of NC, Fe_2O_3(H)-NC, and Al/Fe_2O_3(H)-NC corresponding to the thermal decomposition process at the typical temperature points (T_i, T_e, T_L, T_c, and T_f) is shown in **Figure 10** and **Table 6**. It can be found that the gaseous products detected include CO, NO_2, NO, N_2O, HCHO,

and HCOOH during the decomposition process of NC with and without the Fe_2O_3(H) nanoparticles or Al/Fe_2O_3(H).

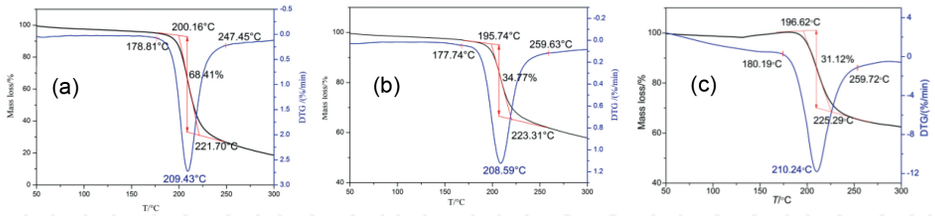

Figure 9. TG-DTG curves of NC (a), Fe_2O_3(H)-NC (b), and Al/Fe_2O_3(H)-NC (c).

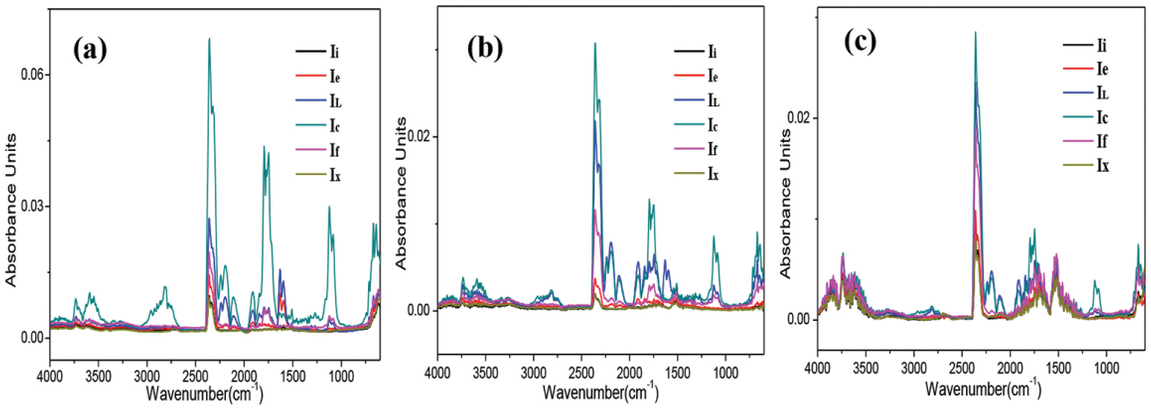

Figure 10. IR spectra of the gases evolved from the degradation of NC (a), Fe_2O_3(H)-NC (b), and Al/Fe_2O_3(H)-NC (c).

NC		Fe_2O_3(H)-NC		Al/Fe_2O_3(H)-NC	
T/°C	Gaseous products	*T*/°C	Gaseous products	*T*/°C	Gaseous products
164.92 (T_x)	H_2O, CO_2	160.47 (T_{x1})	H_2O, CO_2, NO_2	164.40 (T_{x2})	H_2O, CO_2, NO_2, NO
178.81 (T_i)	H_2O, CO_2, NO_2	177.74 (T_{i1})	H_2O, CO_2, NO_2	180.19 (T_{i2})	H_2O, CO_2, NO_2, NO
200.16 (T_e)	H_2O, CO_2, NO_2, NO	195.74 (T_e)	H_2O, CO_2, NO_2, NO	196.76 (T_e)	H_2O, CO_2, NO_2, NO
209.43 (T_L)	H_2O, CO_2, NO_2, NO, N_2O, HCHO, HCOOH	208.59(T_L)	H_2O, CO_2, CO, NO_2, NO, N_2O, HCHO, HCOOH	210.24 (T_L)	H_2O, CO_2, CO, NO_2, NO, N_2O, HCHO, HCOOH
221.70 (T_c)	H_2O, CO_2, CO, NO_2, NO, HCHO, HCOOH	223.31 (T_c)	H_2O, CO_2, CO, NO_2, NO, N_2O, HCHO, HCOOH	225.47 (T_c)	H_2O, CO_2, CO, NO_2, NO, N_2O, HCOOH
247.45 (T_f)	H_2O, CO_2, NO	259.63 (T_f)	H_2O, CO_2, CO, NO, HCOOH	259.72 (T_f)	H_2O, CO_2, NO_2, NO

Note: T_x, some temperature below the initial decomposition temperature; T_{x1}(T_{x2}), some temperature below T_{i1}(T_{i2}); T_i, the initial decomposition temperature; T_{i1}, the initial decomposition temperature of the obvious exothermic peak of Fe_2O_3(H)-NC; T_{i2}, the initial decomposition temperature of the obvious exothermic peak of AL/Fe_2O_3(H)-NC; T_e, the extrapolated onset temperature; T_L, the peak temperature; T_c, the extrapolated end temperature; T_f, the final temperature.

Table 6. Gaseous products generated during the decomposition processes of NC, Fe_2O_3(H)-NC, and Al/Fe_2O_3(H)-NC at different temperatures.

Table 6 lists the gaseous products generated during the decomposition processes of NC, Fe_2O_3(H)-NC, and Al/Fe_2O_3(H)-NC at the typical temperature points. At the initial decomposition temperature (T_i), the IR absorption peaks of H_2O (3600–3740 cm^{-1}), CO_2 (2360, 670 cm^{-1}), and NO_2 (1593–1635 cm^{-1}) [45, 46] are easily identifiable (**Figure 10**(a, I_i) and (b, I_i)). During the whole testing process, the existence of H_2O and CO_2 from the ambience is the outside disruptive factor, which cannot be ignored. In order to prove that H_2O and CO_2 gas detected at 178.81°C are not the products of NC decomposition, the variation of IR absorption peaks at 164.92°C is obtained, which is shown in **Figure 10**(a, I_x). The TG-DTG curves of NC in **Figure 9(a)** show that the decomposition of NC has not occurred at 164.92°C and begins from 178.81°C. By comparing the curves I_x (164.92°C) and I_i (178.81°C) in **Figure 10(a)**, the bands at 3600–3740 cm^{-1} are assigned to O-H-bonding-stretching vibrational modes for water as an impurity because of the extremely similar absorptive intensities. Apart from the impurity peaks of H_2O, it can be concluded that CO_2 gas is not the initial degradation product because the intensities of the detected CO_2 gas are basically unchanged at both 164.92 and 178.81°C shown in **Figure 10**(a, I_x, and I_i). Furthermore, the noticeable IR bands of NO_2 are found in the region of 1593–1635 cm^{-1} at the beginning of the decomposition of NC shown in the curve I_i (**Figure 10(a)**) [46], which means that the NO_2 gas is an initial degradation product. The above results concur with those of several previous studies [22, 23, 47, 48] in which the O-NO_2 bond is deemed to be the first step leading to the release of NO_2

$$\mathrm{RO-NO_2} \rightarrow \mathrm{RO\cdot + -NO_2} \tag{6}$$

The NO_2 stagnates in the polymer skeleton and then reacts with the RO• radical or its degradation products. It is particularly necessary to point out that the signal of NO_2 was present as shown in the IR spectrum in **Figure 10**(b, I_x) at 160.47°C (T_{x1}). The intensities of NO_2 peaks increase with temperature, which is very different from the decomposition of NC. It is a fact that NC could be slowly decomposed as the temperature increases further, which has been enhanced by Fe_2O_3(H) nanoparticles due to their catalysis. That is, the Fe_2O_3(H) nanoparticles could accelerate the O-NO_2 bond cleavage and the release of NO_2. For this reason, the absorption peaks of H_2O and CO_2 exist not only from the environment but also from the degradation of Fe_2O_3(H)-NC at 160.47°C (T_{x1}). Moreover, both NO_2 and NO are detected besides the H_2O and CO_2 gases, which indicates that Al/Fe_2O_3(H) can make NC decompose faster than Fe_2O_3(H) does.

Figure 11 shows the 3D-IR spectra of gas products of NC, Fe_2O_3(H)-NC, and Al/Fe_2O_3(H)-NC at a heating rate of 10°C min^{-1}. At the initial decomposition temperature, the IR absorption peaks of H_2O (3600–3740 cm^{-1}), CO_2 (2360, 670 cm^{-1}), and NO_2 (1593–1635 cm^{-1}) [46, 47] are easily identifiable (**Figure 11**). With the progress of the thermal decomposition process, the gas productions such as NO (1762–1965 cm^{-1}), CO (2194 cm^{-1}), N_2O (2241 cm^{-1}), HCHO (2814 and 1746 cm^{-1}), and HCOOH (1080–1128 cm^{-1}) are detected [26, 47]. By comparing the gaseous products generated during the decomposition processes of NC, Fe_2O_3(H)-NC, and Al/Fe_2O_3(H)-NC at different temperatures, it can be concluded that Fe_2O_3(H) and Al/Fe_2O_3(H) can accelerate the O-NO_2 bond cleavage and the release of NO_2 gas. The evolution of HCOOH

gases is the products of the secondary autocatalytic reactions of NC [24, 26]. From **Figure 11**, the intensities of all these gas products are very strong, which can be taken as an important signal of identifying the faster decomposition rate of Fe_2O_3(H)-NC and Al/Fe_2O_3(H)-NC composites than that of NC. One of the reasons for generating quantities of gases is that the condensed phases break down fast with the presence of Fe_2O_3(H) nanoparticles and Al/Fe_2O_3(H). It has to be pointed out that Al/Fe_2O_3(H) thermite is a better catalyst than Fe_2O_3(H) nanoparticles for reducing the activation energy and accelerating to break the O-NO_2 bond during the thermal decomposition process of NC.

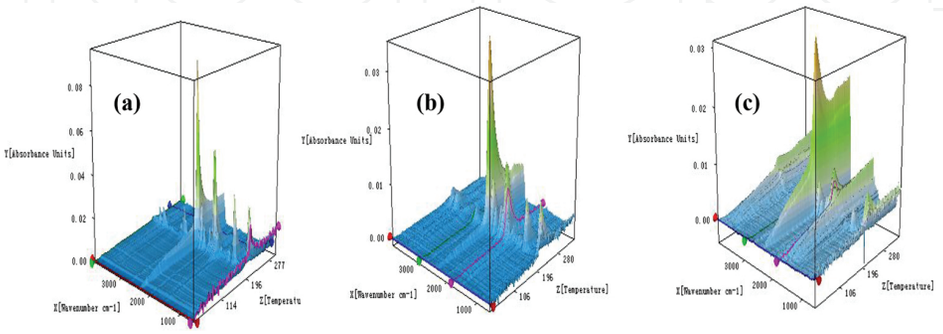

Figure 11. 3D-IR spectra of gas products of NC (a), Fe_2O_3(H)-NC (b), and Al/Fe_2O_3(H)-NC (c) at a heating rate of 10°C min^{-1}.

5. Combustion catalysts used in AP/HTPB propellants

Figure 12 shows the burning rate (u) versus pressure (p) curves of AP/HTPB propellants. Based on the experimental data, the pressure exponent (n) can be calculated [29, 49]. The catalytic efficiency is another evaluation index of the combustion catalyst [29], which is shown in **Figure 13**.

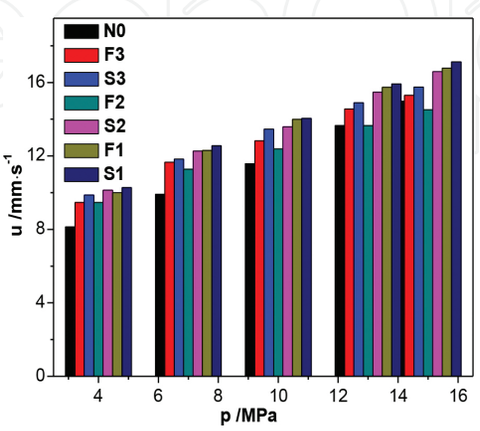

Figure 12. Burning rate (u) versus pressure (p) curves of AP/HTPB composite propellants.

http://dx.doi.org/10.5772/64748

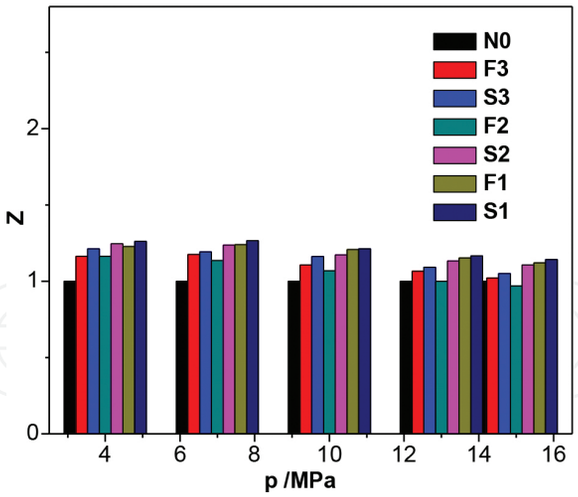

Figure 13. Efficiency of AP/HTPB composite propellants.

The burning rate of all the formulations increases as the pressure rises within 4–15 MPa. For the formulations containing Fe_2O_3, the burning rate is in the order: F2<F3<F1. For the formulations with thermite, that order is S1>S2>S3. The BET-specific surface areas of Fe_2O_3(H), Fe_2O_3(o), and Fe_2O_3(p) are 5.3, 3.1, and 6.9 m^2/g, respectively. Possibly due to the aggregation of Fe_2O_3(H), its specific surface area is smaller than that of Fe_2O_3(p), which is opposite to what we expected simply based on the particle size. However, when the particles are dispersed to the formulations, Fe_2O_3(H) particles are believed to have a larger surface area than Fe_2O_3(p) based on the particle size. Therefore, the superior combustion performance can be ascribed to the dominant role of the surface area of the Fe_2O_3 particles. From **Figures 12** and **13**, the formulations containing thermites all have better burning rate and combustion-supporting ability than the formulations containing the corresponding Fe_2O_3. And thermite with a smaller size of Fe_2O_3 (H) particles has a higher burning rate.

A good formulation is considered to have a high burning rate with a low pressure exponent. From **Table 7**, it can be found that Fe_2O_3 can take effect on decreasing the pressure exponent of the propellant. Considering the role of Al nanopowders and the thermite reaction in enhancing the burning rate, thermites Al/Fe_2O_3 are the better burning rate modifiers in improving the combustion performances of AP/HTPB composite propellants. Overall, the Al/Fe_2O_3(H) is the best combustion catalyst.

p/MPa	n_{N0}	n_{F1}	n_{F2}	n_{F3}	n_{S1}	n_{S2}	n_{S3}
4–7	0.35	0.37	0.31	0.37	0.36	0.34	0.32
7–10	0.42	0.36	0.26	0.27	0.31	0.29	0.36
10–13	0.63	0.45	0.37	0.48	0.48	0.50	0.39
13–15	0.65	0.45	0.43	0.35	0.51	0.49	0.39

Table 7. The burning rate pressure exponent of formulations under different pressure.

Moreover, the combustion wave structures of AP/HTPB composite propellants containing Al/Fe_2O_3 thermite obtained at 4 MPa are shown in **Figure 14**. The flames of the three composites (**Figure 14**) are entirely yellowish that is caused by the fuel-rich diffusion flame generated by the decomposed gases of the binder and the AP particles [50]. There is no obvious dark zone, which is different from the double-base propellants. Above the burning surface, both the AP flame and the diffusion flame produced by the decomposed gases exist simultaneously, leading to major heat release of the combustion process. High flame temperature up to 2700 K was generated at the center of the luminous flame as in the case of Al/Fe_2O_3(H) catalyst. Thick gray smoke was formed surrounding the yellowish flame of the formulation S2, due to the incomplete burning. When adding Al/Fe_2O_3(p) thermite to the AP/HTPB propellants, the front luminous flame of formulation S3 was blown down to the downstream and numerous Fe_2O_3 and Al particles were ejected from the burning surface. The results of the combustion wave structures and flame temperature characteristics indicate that the Al/Fe_2O_3(H)-containing propellant formulation is the best formulation among the tested samples.

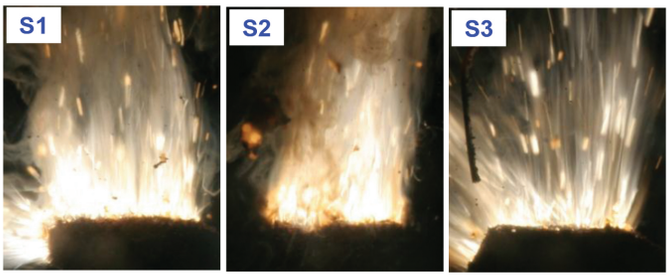

Figure 14. Combustion wave structures of AP/HTPB composite propellants contain thermites Al/Fe_2O_3: (S1) Al/Fe_2O_3(H), (S2) Al/Fe_2O_3(o), and (S3) Al/Fe_2O_3(p).

6. Conclusion

In summary, the structural effect of different sizes and shaped Fe_2O_3 particles on the performance as enhancers, with or without Al, in the thermal decomposition process of NC and the combustion of AP/HTPB has been studied and compared. The as-prepared Fe_2O_3 particles and Al/Fe_2O_3 have good compatibility with NC from DSC thermal analysis, suggesting the safely use of Fe_2O_3-NC and Al/Fe_2O_3-NC composites. The non-isothermal decomposition kinetics of the composites and NC can be modeled by the Avrami-Erofeev equation $f(\alpha)=3(1-\alpha)[-\ln(1-\alpha)]^{1/3}/2$ in differential form. Through the TG-IR analysis of decomposition processes and products of the composites and NC, it is speculated that the as-prepared Fe_2O_3 particles and Al/Fe_2O_3 can effectively accelerate the thermal decomposition reaction rate of NC by promoting the O-NO_2 bond cleavage. Among the three studied different shapes of Fe_2O_3, the granular Fe_2O_3 and its corresponding thermite (Al/Fe_2O_3(H)) exhibit the highest burning rate due to the larger surface area associated with a smaller particle size. Moreover, the Al/Fe_2O_3(H) thermites have more effective combustion-supporting ability for AP/HTPB composite propellants than Fe_2O_3 and the other two as-prepared Al/Fe_2O_3 thermites. Moreover, adding the thermites to

the composite propellants could contribute to increasing the flame temperature and improving the combustion wave structures of the formulations. In all, the addition of the prepared oxides or thermites can distinctly increase the burning rate, enhance the flame temperature, and decrease the burning rate pressure exponent of the AP/HTPB composite propellants.

Acknowledgements

This work was supported by the Program for the National Natural Science Foundation of China (No. 21373161), Research Fund for the Doctoral Program of Higher Education of China (RFDP, No. 20126101110009), and the New Century Excellent Talents in the University of Ministry of Education of China (NCET-12-1047).

Author details

Ningning Zhao[1], Jiachen Li[1], Fengqi Zhao[2], Ting An[2], Rongzu Hu[2] and Haixia Ma[1*]

*Address all correspondence to: mahx@nwu.edu.cn

1 School of Chemical Engineering, Northwest University, Shaanxi Xi'an, P.R. China

2 Science and Technology on Combustion and Explosion Laboratory, Xi'an Modern Chemistry Research Institute, Shaanxi Xi'an, P.R. China

References

[1] Gibot P, Comet M, Eichhorn A, Schnell F, Muller O, Ciszek F, Boehrer Y, Spitzer D. Highly insensitive/reactive thermite prepared from Cr_2O_3 nanoparticles. Propellants, Explosives, Pyrotechnics, 2011, 36(1): 80–87. DOI: 10.1002/prep.201000080.

[2] Pantoya ML, Granier JJ. Combustion behavior of highly energetic thermites: nano versus micron composites. Propellants Explosives Pyrotechnics, 2005, 30(1): 53–62. DOI: 10.1002/prep.200400085.

[3] Shi Y, Guo QJ, Zachariah MR. Electrospun nanofiber based thermite textiles and their reactive properties. ACS Applied Materials & Interfaces, 2012, 4(12): 6432–6435.DOI: 10.1021/am3021125.

[4] Li Y, Song WL, Xie CS, Zeng DW, Wang AH, Hu ML. Influence of humidity on the thermal behavior of aluminum nanopowders. Materials Chemistry and Physics, 2006, 97(1): 127–131. DOI: 10.1016/j.matchemphys.2005.07.064.

[5] An T, Zhao FQ, Hao HX, Ma HX, Yao EG, Yang Y, Tan Y. Effect of thermites on laser ignition characteristics of double base propellants. Chinese Journal of Explosives & Propellants, 2011, 34(1): 67–72. DOI: 1007-7812(2011)01-0067-06.

[6] Martirosyan KS. Nanoenergetic gas-generators: principles and applications. Journal of Materials Chemistry, 2011, 21(26): 9400–9405. DOI: 10.1039/C1JM11300C.

[7] Armstrong RW, Baschung B, Booth DW, Samirant M. Enhanced propellant combustion with nanoparticles. Nano Letters, 2003, 3(2): 253–255. DOI: 10.1021/nl025905k.

[8] Bockmon BS, Pantoya ML, Son SF, Asay BW, Mang JT. Combustion velocities and propagation mechanisms of metastable interstitial composites. Journal of Applied Physics, 2005, 98(6): 064903–064903-7. DOI: 10.1063/1.2058175.

[9] Sullivan K, Young G, Zachariah MR. Enhanced reactivity of nano-B/Al/CuO MIC's. Combustion & Flame, 2009, 156(2): 302–309. DOI: 10.1016/j.combustflame.2008.09.011.

[10] Granier JJ, Plantier KB, Pantoya ML. The role of the Al_2O_3 passivation shell surrounding nano-Al particles in the combustion synthesis of NiAl. Journal of Materials Science, 2004, 39(39): 6421–6431. DOI: 10.1023/B:JMSC.000004.

[11] Wang LL, Munir ZA, Maximov YM. Thermite reactions: their utilization in the synthesis and processing of materials. Journal of Materials Science, 1993, 28(14): 3693–3708. DOI: 10.1007/BF00353167.

[12] Zhou L, Piekiel N, Chowdhury S, Zachariah MR. Time-resolved mass spectrometry of the exothermic reaction between nanoaluminum and metal oxides: the role of oxygen. Journal of Physical Chemistry C, 2010, 114(33): 14269–14275. DOI: 10.1021/jp101146a.

[13] Ulrich T. Energetic Materials: Particle Processing and Characterization. Printed in the Federal Republic of Germany. Wiley-VCH Verlag GmbH & Co. KGaA, Weinheim, 2005: i–xxii. DOI: 10.1002/3527603921.

[14] Jayaraman K, Anand KV, Chakravarthy SR, Sarathi R. Effect of nano-aluminium in plateau-burning and catalyzed composite solid propellant combustion. Combustion & Flame, 2009, 156(8): 1662–1673. DOI: 10.1016/j.combustflame.2009.03.014.

[15] Galfetti L, De Luca LT, Severini F, Meda L, Marra G, Marchetti M, Regi M, Bellucci S. Nanoparticles for solid rocket propulsion. Journal of Physics Condensed Matter, 2006, 18(33): S1991–S2005(15). DOI: 10.1088/0953-8984/18/33/S15.

[16] Patil PR, Krishnamurthy VN, Joshi SS. Differential scanning calorimetric study of HTPB based composite propellants in presence of nano ferric oxide. Propellants Explosives Pyrotechnics, 2006, 31(31): 442–446. DOI: 10.1002/prep.200600059.

[17] Meda L, Marra G, Galfetti L, Severini F, De Luca L. Nano-aluminum as energetic material for rocket propellants. Materials Science & Engineering C, 2007, 27(5): 1393–1396. DOI: 10.1016/j.msec.2006.09.030.

[18] Sun DP, Ma B, Zhu CL, Liu CS, Yang JZ. Novel nitrocellulose made from bacterial cellulose. Journal of Energetic Materials, 2010, 28(28): 85–97. DOI: 10.1080/07370650903222551.

[19] Liu S, Ye M, Han A, Chen X. Preparation and characterization of energetic materials coated superfine aluminum particles. Applied Surface Science, 2014, 288(7): 349–355. DOI: 10.1016/j.apsusc.2013.10.031.

[20] Yi JH, Zhao FQ, Hu RZ, Xue L, Xu SY. Thermal safety study on TEGDN/NG/NC gun propellant. Journal of Energetic Materials, 2010, 28(4): 285–298. DOI: 10.1080/07370651003785695.

[21] López-López M, Ferrando JL, García-Ruiz C. Dynamite analysis by Raman spectroscopy as a unique analytical tool. Analytical chemistry, 2013, 85(5): 2595–2600. DOI: 10.1021/ac302774w.

[22] Konkin AL, Ershov BG, Kargin YM, Chichirov AA, Agafonov MN. Study of the radical products of the thermal decomposition of nitrocellulose. Russian Chemical Bulletin, 1989, 38(11): 2426–2428. DOI: 10.1007/BF01168105.

[23] Makashir PS, Mahajan RR, Agrawal JP. Studies on kinetics and mechanism of initial thermal decomposition of nitrocellulose. Journal of Thermal Analysis, 1995, 45(3): 501–509. DOI: 10.1007/BF02548782.

[24] Shehata AB, Hassan MA, Nour MA. Effect of new poly 2-acryloyl-N, N′-bis (4-nitrophenyl) propandiamide and poly 2-acryloyl-N, N′-bis (4-methylphenyl) propandiamide and their synergistic action on the stability of nitrocellulose. Journal of Hazardous Materials, 2003, 102(2): 121–136.

[25] Katoh K, Higashi E, Nakano K, Ito S, Wada Y, Kasamatsu J, Miya H, Yamamoto M, Wada Y, Thermal behavior of nitrocellulose with inorganic salts and their mechanistic action. Propellants Explosives Pyrotechnics, 2010, 35: 461–467. DOI: 10.1016/S0304-3894(03)00138-9.

[26] Chen JK, Brill TB. Thermal decomposition of energetic materials 50. Kinetics and mechanism of nitrate ester polymers at high heating rates by SMATCH/FTIR spectroscopy. Combustion & Flame, 1991, 85(s3–4): 479–488. DOI: 10.1016/0010-2180(91)90149-6.

[27] Mahajan RR, Makashir PS, Agrawal JP. Combustion behaviour of nitrocellulose and its complexes with copper oxide. hot stage microscopic studies. Journal of Thermal Analysis & Calorimetry, 2001, 65(3): 935–942. DOI: 10.1023/A:1011905021880.

[28] Yang Y, Ma HX, Zhuang J, Wang X. Morphology-controlled synthesis of hematite nanocrystals and their facet effects on gas-sensing properties. Inorganic Chemistry, 2011, 50(20): 10143–10151. DOI: 10.1021/ic201104w.

[29] Zhao NN, He CC, Liu JB, Gong HJ, An T, Xu HX, Zhao FQ, Hu RZ, Ma HX, Zhang JZ. Dependence of catalytic properties of Al/Fe_2O_3 thermites on morphology of Fe_2O_3

particles in combustion reactions. Journal of Solid State Chemistry, 2014, 219: 67–73. DOI: 10.1016/j.jssc.2014.06.039.

[30] Daniel P, Pantoya ML, Clapsaddle BJ. Effect of nanocomposite synthesis on the combustion performance of a ternary thermite. Journal of Physical Chemistry B, 2005, 109(43): 20180–20185.

[31] Fu YY, Wang RM, Xu J, Chen J, Yan Y, Narlikar AV, Zhang H. Synthesis of large arrays of aligned α-Fe_2O_3 nanowires. Chemical Physics Letters, 2003, 379(3): 373–379. DOI: 10.1016/j.cplett.2003.08.061.

[32] Zhu D, Chen YL, Miller RA. Defect clustering and nano-phase structure characterization of multi-component rare earth oxide doped zirconia-yttria thermal barrier coatings. Ceramic Engineering & Science Proceedings, 1990, 24(3): 525–534. DOI: 10.1002/9780470294802.ch75.

[33] Gotić M, Dražić G, Musić S. Hydrothermal synthesis of α-Fe_2O_3 nanorings with the help of divalent metal cations, Mn^{2+}, Cu^{2+}, Zn^{2+} and Ni^{2+}. Journal of Molecular Structure, 2011, 993(1): 167–176. DOI: 10.1016/j.molstruc.2010.12.063.

[34] Apte SK, Naik SD, Sonawane RS, Kale BB, Baeg JO. Synthesis of nanosize-necked structure α- and γ-Fe_2O_3 and its photocatalytic activity. Journal of the American Ceramic Society, 2007, 90(90): 412–414. DOI: 10.1111/j.1551-2916.2006.01424.x.

[35] Woo K, Lee HJ, Ahn JP, Park YS. Sol–gel mediated synthesis of Fe_2O_3 nanorods. Advanced Materials, 2003, 15(20): 1761–1764. DOI: 10.1002/adma.200305561.

[36] Khan SB, Faisal M, Rahman MM, Abdel-Latif IA, Ismail AA, Akhtar K, Al-Hajry A, Asiri AM, Alamry KA. Highly sensitive and stable phenyl hydrazine chemical sensors based on CuO flower shapes and hollow spheres. New Journal of Chemistry, 2013, 37(4): 1098–1104. DOI: 10.1039/C3NJ40928G.

[37] Aghaie-Khafri M, Lafdani MHK. A novel method to synthesize Cr_2O_3 nanopowders using EDTA as a chelating agent. Powder Technology, 2012, 222: 152–159. DOI: 10.1016/j.powtec.2012.02.024.

[38] Pei Z, Zhang Y. A novel method to prepare Cr_2O_3 nanoparticles. Materials Letters, 2008, 62(3): 504–506. DOI: 10.1016/j.matlet.2007.05.073.

[39] Ma HX, Yan B, Ren YH, Guan YL, Zhao FQ, Song JR, Hu RZ. Thermal behavior and thermal safety on 3,3-dinitroazetidinium salt of perchloric acid. Journal of Thermal Analysis and Calorimetry, 2011, 103(2): 569–575. DOI: 10.1007/s10973-010-0950-2.

[40] Ma HX, Zhao NN, Yan B, Guan YL, Li JF, Song JR. Molecular structure, quantum chemical investigation, and thermal behavior of $(DNAZ\text{-}CO)_2$. Journal of Structural Chemistry, 2012, 53(3): 534–541. DOI: 10.1134/S0022476612030171.

[41] Ma HX, Yan B, Li ZN, Song JR, Hu RZ. Synthesis, molecular structure, non-isothermal decomposition kinetics and adiabatic time to explosion of 3,

3-dinitroazetidinium 3, 5-dinitrosalicylate. Journal of Thermal Analysis and Calorimetry, 2009, 95(2): 437–444. DOI: 10.1007/s10973-008-9255-0.

[42] Ma HX, Yan B, Li ZN, Guan YL, Song JR, Xu KZ, Hu RZ. Preparation, non-isothermal decomposition kinetics, heat capacity and adiabatic time-to-explosion of NTO DNAZ. Journal of Hazardous Materials, 2009, 169(1): 1068–1073. DOI: 10.1016/j.jhazmat.2009.04.057.

[43] Ma HX, Song JR, Zhao FQ, Hu RZ, Xiao HM. Nonisothermal decomposition kinetics and computational studies on the properties of 2,4,6,8-tetranitro-2,4,6,8-tetraazabicyclo [3,3,1] onan-3,7-dione (TNPDU). Journal of Physical Chemistry A, 2007, 111(35): 8642–8649. DOI: 10.1021/jp073092o.

[44] Zhang TL, Hu RZ, Xie Y, Li FP. The estimation of critical temperatures of thermal explosion for energetic materials using non-isothermal DSC. Thermochimica Acta, 1994, 244: 171–176. DOI: 10.1016/0040-6031(94)80216-5.

[45] Li Y, Chenxia K, Huang C, Chen Y. Effect of MnC_2O_4 nanoparticles on the thermal decomposition of TEGDN/NC propellant. Journal of Thermal Analysis and Calorimetry, 2011, 109(1): 171–176. DOI: 10.1007/s10973-011-1694-3.

[46] Dong Q. Infrared Spectrometry. Beijing: Petroleum Chemical Industry Press; 1977. p. 165–170.

[47] Gratien A, Nilsson E, Doussin JF, Johnson MS, Nielsen CJ, Stenstrom Y, Picquet-Varrault B. UV and IR absorption cross-sections of HCHO, HCDO, and DCDO. Journal of Physical Chemistry A, 2007, 111(45): 11506–11513. DOI: 10.1021/jp074288r.

[48] Fan RH, Lü HL, Sun KN, Wang WX, Yi XB. Kinetics of thermite reaction in Al-Fe_2O_3 system. Thermochimica Acta, 2006, 440(2): 129–131. DOI: 10.1016/j.tca.2005.10.020.

[49] Stephens MA, Petersen EL, Carro R, Reid DL, Seal S. Multi-parameter study of nanoscale TiO_2 and CeO_2 additives in composite AP/HTPB solid propellants. Propellants, Explosives, Pyrotechnics, 2010, 35(2): 143–152. DOI: 10.1002/prep.200800104.

[50] Kubota TKN. Low pressure burning of ammonium perchlorate composite propellants. Combustion Science & Technology, 1986, 47(1): 81–91. DOI: 10.1080/00102208608923866.

IntechOpen